

Statistical analysis of random trajectories of vibrated disks: Towards a macroscopic realization of Brownian motion

Yann Lanoiselée,^{1,*} Guillaume Briand,^{2,†} Olivier Dauchot,^{2,‡} and Denis S. Grebenkov^{1,3,§}

¹Laboratoire de Physique de la Matière Condensée (UMR 7643), CNRS–Ecole Polytechnique, University Paris-Saclay, 91128 Palaiseau, France

²Laboratoire Gulliver, UMR CNRS 7083, ESPCI Paris, PSL University, 10, rue Vauquelin, 75231 Paris cedex 05, France

³Interdisciplinary Scientific Center Poncelet (ISCP), Bolshoy Vlasyevskiy Pereulok 11, 119002 Moscow, Russia[¶]



(Received 1 December 2017; revised manuscript received 22 October 2018; published 10 December 2018)

We propose a macroscopic realization of planar Brownian motion by vertically vibrated disks. We perform a systematic statistical analysis of many random trajectories of individual disks. The distribution of increments is shown to be almost Gaussian, with slight deviations at large increments caused by interdisk collisions. The velocity autocorrelation function takes both positive and negative values at short lag times but rapidly vanishes. We compare the empirical and theoretical distributions of time-averaged mean-squared displacements and discuss distinctions between their mean and mode. These well-controlled experimental data can serve for validating various statistical tools developed for the analysis of single-particle trajectories in microbiology.

DOI: [10.1103/PhysRevE.98.062112](https://doi.org/10.1103/PhysRevE.98.062112)

I. INTRODUCTION

One of the first reports of Brownian motion is attributed to the Scottish botanist Robert Brown who observed in a microscope a continuous jittery motion of minute particles ejected from *Clarkia* pollen grains suspended in water [1]. Since a more systematic study by Jean Perrin [2,3], the abundant experimental evidence of Brownian motion of microscopic particles has been established [4–7]. The mathematical origin of this abundance lies in the central limit theorem which implies a universal probabilistic description of motion at mesoscopic time and length scales, regardless of microscopic dynamics. In turn, experimental observations of Brownian motion in the macroscopic world are rarer. In fact, it is quite difficult to design an experiment with macroscopic objects that would result in Brownian trajectories. On one hand, the motion is strongly influenced by inertial effects, resulting in ballistic segments of the trajectory at the macroscopic scale (e.g., the motion of billiard balls). On the other hand, the number of interacting objects in a macroscopic system is much smaller than the number of water molecules involved in the motion of a microscopic particle, whereas the separation between the timescale of an elementary displacement and the duration of the measurement is not large enough. As a consequence, the motion of macroscopic objects is not randomized enough by their collisions. In particular, the dynamics of granular matter is typically far from Brownian motion [8–13]. For instance,

there is a rather narrow range of packing fractions, for which the motion of spherical beads is fluid-like: in the low-density regime, collisions between beads are rare while the mean-free path is long so that too large experimental setups would be needed to observe a Brownian trajectory; in the high-density regime, interbead collisions are frequent but collective modes of motion (e.g., crystallization or jamming) become dominant. In other words, one needs specifically designed experiments to realize Brownian motion at macroscopic scales [14].

From the practical point of view, a well-controlled experimental realization of a macroscopic diffusive motion with an excellent statistics of long trajectories can serve as a benchmark for testing various statistical tools developed for the analysis of single-particle trajectories (see [15–28] and references therein). In fact, it is essential to disentangle finite time average and finite sampling effects when performing single-probe experiments in biology (e.g., the intracellular transport or the motion of proteins on cell membranes). While statistical tools are commonly tested on simulated trajectories, a macroscopic realization of diffusive motions can present a rare opportunity to confront simulations and theoretical results to an experimental situation with true experimental noises, uncertainties, resolution issues, etc.

In this paper, we report an experimental observation of the diffusive motion realized by macroscopic disks of 4 mm diameter on a vertically vibrating plate (see Sec. II). Vibrations pump into the system the kinetic energy that substitutes thermal energy that drives the motion in a microscopic system. We undertake a systematic statistical analysis of the acquired trajectories of individual disks (Sec. III). In particular, we analyze the distribution of one-step displacements, the ergodicity, the velocity autocorrelation function, and the distribution of time-averaged mean-square displacements (TAMSD). This analysis shows that the macroscopic motion of disks exhibits small deviations from Brownian motion at short times but approaches it at longer times. We also discuss

*yann.lanoiselee@polytechnique.edu

†guillaume.briand@espci.fr

‡olivier.dauchot@espci.fr

§denis.grebenkov@polytechnique.edu

¶International Joint Research Unit: UMI 2615 CNRS, IUM, IITP RAS, Steklov MI RAS, Skoltech, and HSE, Moscow, Russian Federation.

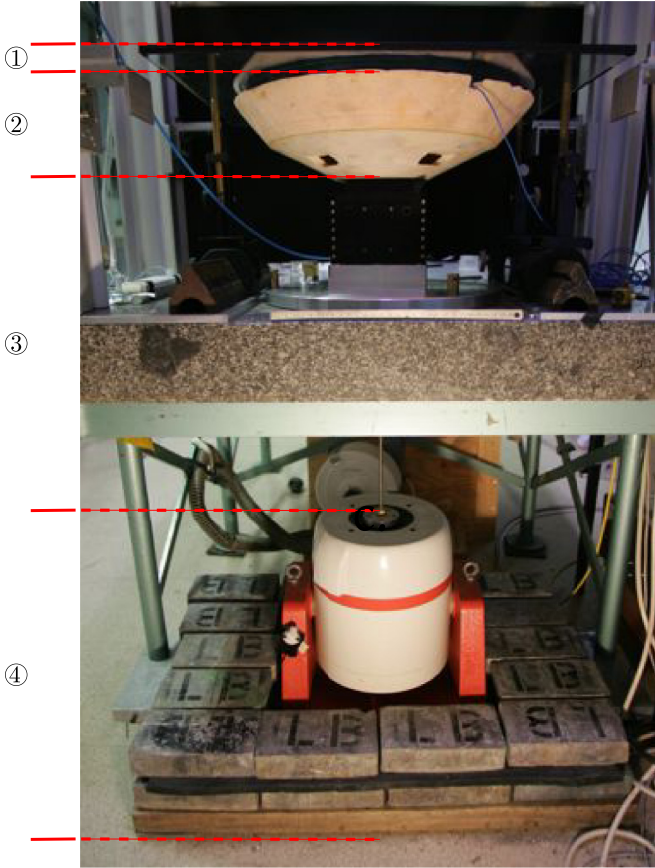


FIG. 1. View of the experimental setup. The vibration is provided by an electromagnetic servo-controlled shaker ballasted with lead and isolated from ground by rubber mats (4). It is then transmitted to the vibrating plate (2) via a brass rod coupled to a square air bearing (3). The vibrating plate (2) is composed of a nylon plate, an expanded polystyrene truncated cone, on top of which is glued the glass plate which supports the vibrated disks. Finally, the disks are confined vertically by a top glass plate fixed to an external rigid frame (1) (reproduced from [29]).

the impact of static and dynamic noises onto the statistical estimation.

II. EXPERIMENTAL SETUP

The experimental system, made of vibrated disks, has been described in detail previously [29]. We recall here the key ingredients of the setup (see Fig. 1). Experiments with shaken granular particles are notoriously susceptible to systematic deviations from pure vertical vibration and special care must be taken to avoid them. First, to ensure the rigidity of the tray supporting the particles, we use a 110 mm thick truncated cone of expanded polystyrene sandwiched between two nylon disks. The top disk (diameter 425 mm) is covered by a glass plate on which lie the particles. The bottom one (diameter 100 mm) is mounted on the slider of a stiff square air bearing (C40-03100-100254, IBSPE), which provides virtually friction-free vertical motion and submicron amplitude residual horizontal motion. The vertical alignment is controlled by set screws. The vibration is produced with an electromagnetic

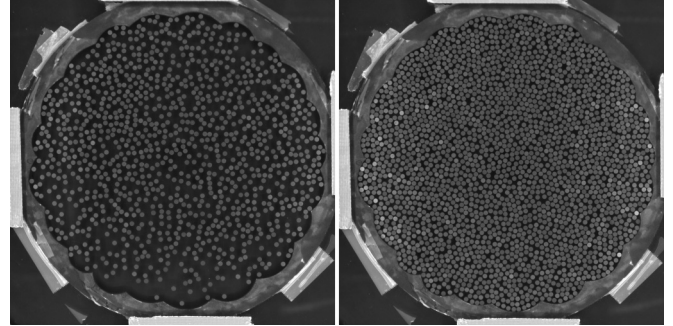


FIG. 2. Two snapshots of the disks on a vibrated plate as recorded by the CCD camera, at the lowest packing density $\phi \approx 0.298$ (left) and at the highest packing density $\phi \approx 0.637$ (right). The diameter of the arena is 320 mm, whereas the diameter of each disk is 4 mm. Only the disks within a central circular region of interest of diameter 200 mm far from the border of the arena were taken into our statistical analysis.

servo-controlled shaker (V455/6-PA1000L, LDS), the accelerometer for the control being fixed at the bottom of the top vibrating disk, embedded in the expanded polystyrene. A 400 mm long brass rod couples the air-bearing slider and the shaker. It is flexible enough to compensate for the alignment mismatch, but stiff enough to ensure mechanical coupling. The shaker rests on a thick wooden plate ballasted with 460 kg of lead bricks and isolated from the ground by rubber mats (MUSTshock 100 × 100 × EP5, Musthane). We have measured the mechanical response of the whole setup and found no resonances in the window 70–130 Hz. We use a sinusoidal vibration of frequency $f = 95$ Hz and set the relative acceleration to gravity $\Gamma = a(2\pi f)^2/g = 2.4$, where the vibration amplitude a at a peak acceleration is 100 μm . Using a triaxial accelerometer (356B18, PCB Electronics), we checked that the horizontal to vertical ratio is lower than 10^{-2} and that the spatial homogeneity of the vibration is better than 1%.

The particles are micromachined copper-beryllium disks (diameter $d = 4 \pm 0.03$ mm). The contact with the vibrating plate is that of an extruded cylinder, resulting in a total height $h = 2.0$ mm. They are sandwiched between two thick glass plates separated by a gap $H = 2.4$ mm and laterally confined in an arena of diameter 320 mm (Fig. 2). A CCD camera with a spatial resolution of 1728×1728 pixels and standard tracking software is used to capture the motion of the disks at a frame rate of 25 Hz. In a typical experiment, the motion of the disks is recorded during 600 seconds, producing 15 000 images. The resolution on the position x of the disks is better than 0.05 disk diameter (i.e., 0.2 mm).

In the following, disk trajectories are tracked within a circular region of interest (ROI) of diameter $50d = 200$ mm far from the border of the arena, where the long-time averaged density field is homogeneous. The average packing fraction ϕ measured inside the ROI ranges from 0.3 to 0.64, and the total number of disks ranges from 1000 to 2500. As the onset of spatial order typically takes place at $\phi_{\dagger} \simeq 0.71$, we always deal with a liquid state.

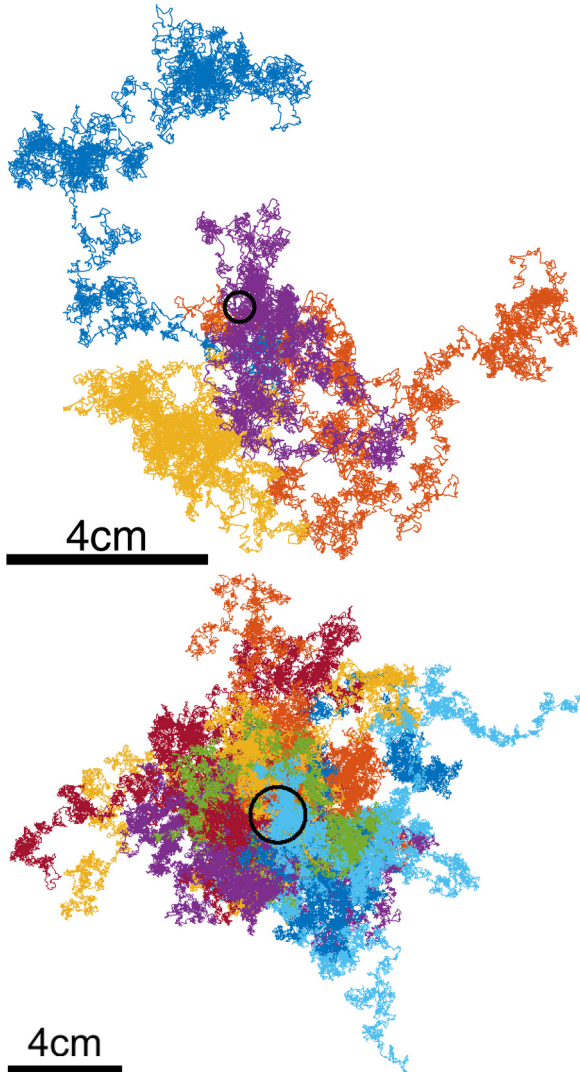


FIG. 3. Top: Example of random trajectories of 4 disks that were originally located close to each other (inside the black circle) and then diffused during 600 seconds (i.e., 15 000 points in each trajectory). Bottom: Example of random trajectories of 34 disks that were originally located close to each other and then diffused during 464.6 seconds (i.e., 11 615 points in each trajectory). Both examples come from the sample 1 with the lowest packing density.

III. STATISTICAL ANALYSIS

We performed a systematic statistical analysis of the acquired random trajectories. Examples of such trajectories are shown in Fig. 3 (three videos of the collective motion of vibrated disks are provided in the Supplemental Material [30]).

A. Data description

We analyzed 14 samples with different surface packing fractions ϕ , ranging between 0.298 and 0.637 (Table I). The time step (i.e., the duration of one displacement) is fixed by the acquisition frequency: $\delta = 1/(25 \text{ Hz}) = 0.04 \text{ s}$. The positions are measured in units of the disk diameter, $d = 4 \text{ mm}$. To avoid boundary effects, only the disks within the

TABLE I. Summary of experimental data: the sample index, the surface fraction ϕ , the standard deviation σ of one-step one-dimensional increments (in units of the disk diameter $d = 4 \text{ mm}$), and the corresponding diffusion coefficient: $D = \sigma^2/(2\delta)$, with $\delta = 0.04 \text{ s}$. The values after the sign \pm specify the standard deviation of this basic diffusivity estimator among different trajectories. The last column shows the diffusion coefficient estimated by accounting for localization errors and motion blur; see Sec. IIIH. The zeroth sample corresponds to a reference experiment with a single disk. Note that the maximal disk packing fraction, corresponding to the close-packed hexagonal lattice, is $\pi/(2\sqrt{3}) \simeq 0.9069$, while the crystallization transition for equilibrium hard disks takes place at $\phi^\dagger \simeq 0.71$; as a consequence, all our samples are in a fluid-like state.

Sample	ϕ	σ/d	$D (\text{mm}^2/\text{s})$	$D_{\text{opt}} (\text{mm}^2/\text{s})$
0		0.115	2.7 ± 0.1	5.1 ± 0.3
1	0.298	0.096	1.8 ± 0.1	2.7 ± 0.2
2	0.324	0.094	1.8 ± 0.1	2.6 ± 0.2
3	0.350	0.093	1.8 ± 0.1	2.6 ± 0.2
4	0.376	0.105	2.2 ± 0.1	3.2 ± 0.3
5	0.402	0.103	2.1 ± 0.1	2.9 ± 0.3
6	0.428	0.111	2.5 ± 0.1	3.4 ± 0.3
7	0.454	0.105	2.2 ± 0.1	3.0 ± 0.2
8	0.480	0.101	2.0 ± 0.1	2.6 ± 0.2
9	0.507	0.098	1.9 ± 0.1	2.4 ± 0.2
10	0.533	0.095	1.8 ± 0.1	2.2 ± 0.2
11	0.559	0.093	1.7 ± 0.1	2.0 ± 0.2
12	0.585	0.094	1.8 ± 0.1	2.0 ± 0.1
13	0.611	0.094	1.7 ± 0.1	1.8 ± 0.2
14	0.637	0.090	1.6 ± 0.1	1.6 ± 0.1

ROI were used for the analysis. In particular, a trajectory is terminated when the disk leaves the ROI, and a new trajectory is initiated when a disk enters the ROI. As a consequence, the acquired trajectories have very different lengths varying from 1 to 15 000. To improve the statistical accuracy of our results, we discarded all the trajectories of length shorter than 1000. In Appendix A, we checked that the selection bias of this removal procedure is negligible in our experiment. The disks exhibited multiple mutual collisions during the experiments. Although the collective motion of these disks might be studied as the dynamics of interacting particles in a large phase space, we look at this problem from the single-particle point of view and treat each disk as a single particle interacting with its complex dynamic environment. This view is typical for single-particle tracking experiments in microbiology when one can record only the motion of a labeled (e.g., fluorescent) particle, whereas the dynamics of all other constituents of the cytoplasm remains inaccessible.

B. Distribution of increments

We start by verifying whether the one-step increments obey a Gaussian distribution. For each sample, we collected the one-step increments along X and Y axes for each trajectory in the sample and constructed their histogram. Having checked for the isotropy of the statistics, we focus on one-dimensional increments and merge increments along X and Y coordinates in order to get a representative statistics even for large

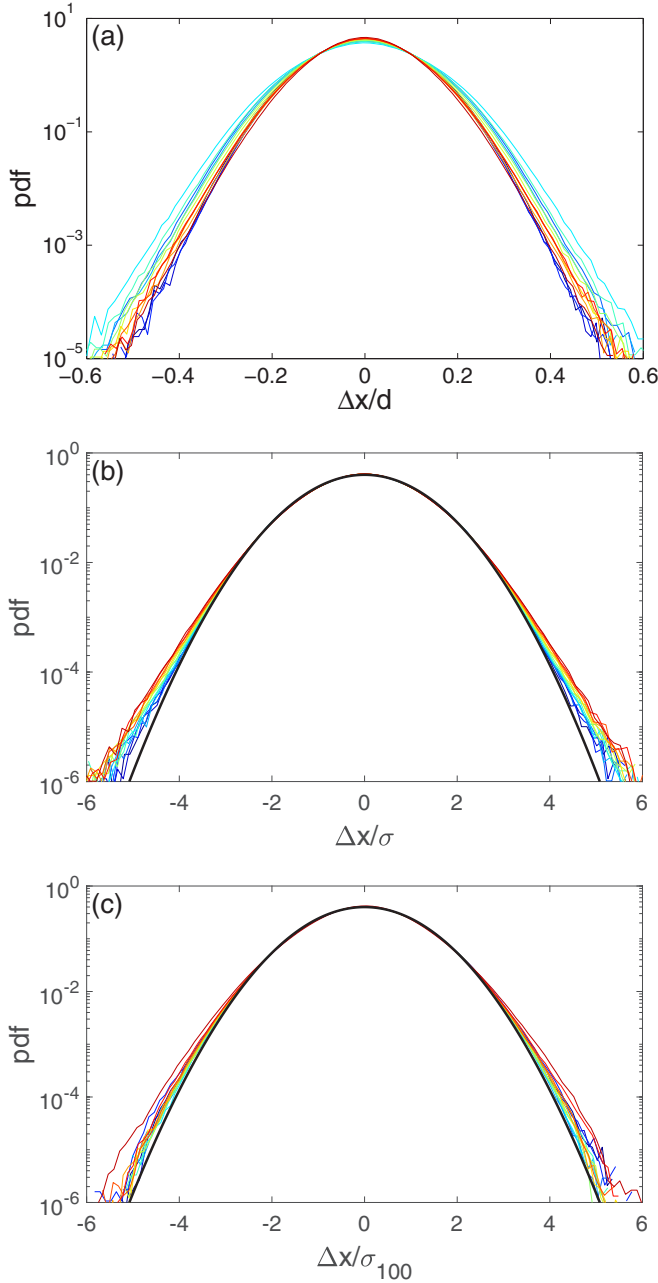


FIG. 4. (a) Empirical distributions of one-step one-dimensional increments for 14 samples (in units of the disk diameter, $d = 4$ mm). (b) Empirical distributions of rescaled one-step increments for 14 samples. Thick black curve shows the standard Gaussian density $e^{-x^2/2}/\sqrt{2\pi}$. Color of thin curves changes from dark blue for the lowest packing fraction ϕ to dark red for the highest one. (c) Empirical distributions of rescaled one-hundred-step increments for 14 samples.

increments. Figure 4(a) shows these histograms (presented in the form of probability densities at the semilogarithmic scale) for 14 samples. These densities are close to each other and exhibit a parabolic shape reminiscent of a Gaussian distribution. The standard deviations of one-step increments are summarized in Table I. These values are also close to each other and show no systematic dependence on the packing

fraction. At first sight, there is no systematic variation of probability densities with the packing fraction. This suggests that the randomness of motion essentially comes from the rotational symmetry of each disk, which undergoes a displacement in a random direction after each kick by the vibrating plate. This statement is also confirmed by the analysis of several trajectories of a single disk on the vibrated plate (see Appendix B). Note that the frequency of plate vibrations is 4 times higher than the acquisition frequency meaning that each displacement results from 4 random kicks.

Despite their delicate machining, the precise contact of the disks with the vibrating plate is influenced by minor asperities, which differ from disk to disk but also depend on the location of the disks on the vibrating plate. In order to reduce these factors of diversity, we rescale the one-step increments of each trajectory by the empirical standard deviation of these increments (i.e., this rescaling is performed individually for each trajectory and then the increments of all trajectories in a given sample are merged to estimate their distribution). Such a rescaling partly levels off eventual heterogeneities between trajectories. Once calculated, the rescaled increments along X and Y coordinates are merged from different trajectories in each sample. The obtained distributions are presented in Fig. 4(b). One can see that the distributions for all 14 samples almost collapse and remain close to the standard Gaussian density $\exp(-x^2/2)/\sqrt{2\pi}$. However, now that heterogeneities between trajectories have been leveled off by the rescaling, one distinguishes small but systematic and statistically significant deviations for large increments. These deviations progressively increase with the packing fraction, and can therefore be attributed to interdisk collisions. Finally, Fig. 4(c) shows the distribution of rescaled one-hundred-step increments (i.e., with the lag time 100). As each such increment can be seen as the sum of 100 weakly correlated one-step increments, their distribution is expected to be closer to the Gaussian curve. One can see that deviations at large increments are indeed reduced but still present at high packing fractions.

C. Ergodicity hypothesis

We analyze whether the system of vibrated disks can be considered as being at equilibrium. In practice, we test the ergodicity hypothesis which is a necessary but not sufficient condition for equilibrium. The ergodicity hypothesis claims that the ensemble average over many particles is equal to the time average over an (infinitely) long trajectory of one particle. Under the stationarity hypothesis of the increments, we employ the ergodicity estimator $\hat{F}_\omega(n)$ [26,27],

$$\hat{F}_\omega(n) \equiv \frac{1}{n} \sum_{k=1}^n \hat{E}_\omega(k), \quad (1)$$

with

$$\begin{aligned} \hat{E}_\omega(n) \equiv & \frac{1}{N-n+1} \sum_{k=0}^{N-n} e^{i\omega[X(k+n)-X(k)]} \\ & - \frac{1}{N(N+1)} \left| \sum_{k=0}^N e^{i\omega[X(k)-X(0)]} \right|^2 + \frac{1}{N}, \end{aligned} \quad (2)$$

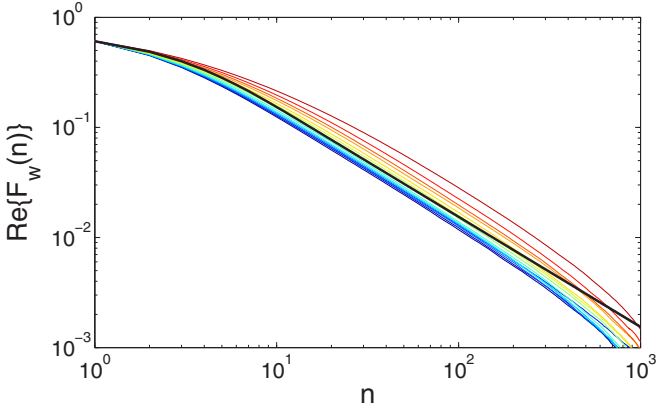


FIG. 5. The real part of the ergodicity estimator, $\text{Re}\{\hat{F}_\omega(n)\}$ (with $\omega = 1/\sigma$), averaged over all trajectories in each of 14 samples (thin lines). Color of thin curves changes from dark blue for the lowest packing fraction ϕ to dark red for the highest one. Thick black line shows the mean value of this estimator for Brownian motion.

where $X(k)$ are successive X coordinates of the points \mathbf{x}_k along a given trajectory of length N (the same analysis was performed for the Y coordinate, not shown). The first term can be interpreted as the time-averaged characteristic function of the increment $X(k+n) - X(k)$ at lag time n , while the second term ensures that the estimator is strictly 0 for a constant process $X(k) = X_0$ [in addition, the mean estimator is strictly 0 for a process with independent $X(k)$]. For Brownian motion, the mean value of the estimator is [27]

$$\mathbb{E}\{\hat{F}_\omega(n)\} = q \frac{1 - q^n}{n(1 - q)} + O(1/N), \quad (3)$$

where $q = e^{-\omega^2\sigma^2/2}$ and σ is the standard deviation of one-step increments. To eliminate the effect of length scale, we set $\omega = 1/\sigma$ that is equivalent to rescaling the trajectory by the standard deviation σ .

Figure 5 shows the real part of the ergodicity estimator averaged over all the trajectories in each of 14 samples. For small n , the higher the packing fraction, the slower the decrease of the estimator with n . Although rigorous statements on ergodicity are only possible for infinitely long trajectories, vanishing of the estimator at large n strongly favors the ergodicity hypothesis. Moreover, for large n , the $1/n$ scaling predicted in the case of Brownian motion (black curve) is recovered. The observed deviations from the black curve suggest that the ergodicity estimator is sensitive even to weak deviations of a studied process from Brownian motion that can be explored in the future as a potential alternative to conventional statistical tests (see, e.g., [21]).

D. Velocity autocorrelations

We also study the velocity autocorrelation function (VACF), which is defined as

$$C(t) = \mathbb{E}\{\mathbf{v}(t) \cdot \mathbf{v}(0)\}, \quad (4)$$

where $\mathbf{v}(t)$ is the velocity at time t . In the experimental setting, the positions are recorded with the time step $\delta = 0.04$ s, so that $t = n\delta$, and the velocity is proportional to the

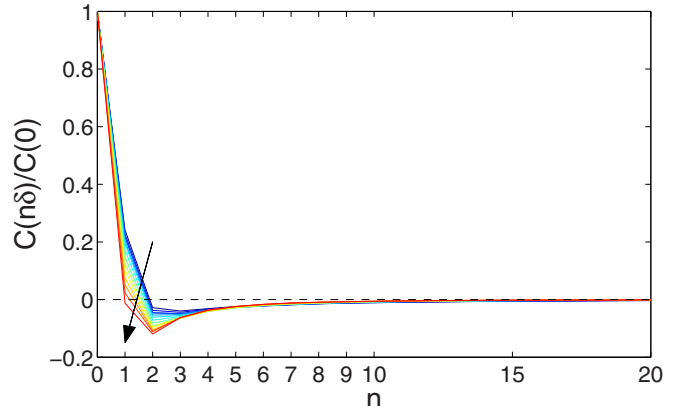


FIG. 6. The normalized VACF, $C(n\delta)/C(0)$, as a function of the lag time n , for 14 samples. Color changes from dark blue for the lowest packing fraction ϕ to dark red for the highest one. This change is also indicated by an arrow.

one-step increment: $\mathbf{v}(n\delta) = (\mathbf{x}_{n+1} - \mathbf{x}_n)/\delta$, with $\mathbf{x}_n = \mathbf{x}(n\delta)$. To improve statistics, we combine the time average along the trajectory of each disk and the ensemble average over many trajectories:

$$C(n\delta) = \frac{1}{M\delta^2} \sum_{m=1}^M \frac{1}{N_m - n - 1} \sum_{k=1}^{N_m - n - 1} (\Delta\mathbf{x}_n^{(m)} \cdot \Delta\mathbf{x}_k^{(m)}), \quad (5)$$

where $\Delta\mathbf{x}_n^{(m)} = \mathbf{x}_{n+1}^{(m)} - \mathbf{x}_n^{(m)}$ is the n th one-step increment of the m th disk, M is the number of disks in a sample, and N_m is the length of the m th trajectory.

Figure 6 shows the normalized VACF, $C(n\delta)/C(0)$, which varies between -1 and 1 , as a function of the lag time n . For all considered samples, the VACF rapidly decreases with time and becomes close to zero for $n \gtrsim 10$. By construction, the normalized VACF is equal to 1 at $n = 0$. Positive auto-correlations at lag time $n = 1$ can potentially be attributed either to inertial effects or to measurement imperfections (see Sec. III H for details). The negative autocorrelations observed for $n > 1$ take their root in an excess of reverse bouncing of the disks when they successively hit the trail, but not only. Since they become more pronounced when the packing fraction increases, they should also come from collisions. In all cases, although the successive increments exhibit small but noticeable correlations, they drop very rapidly as the lag time increases. We recall that the normalized VACF for a discrete-time Brownian motion (a random walk) is 1 for $n = 0$ and 0 otherwise. Strictly speaking, the disk trajectories acquired at time step $\delta = 0.04$ s are therefore not Brownian but remain close to Brownian ones.

E. Estimation of diffusion coefficient

Now we focus on the time-averaged mean-squared displacement (TAMSD), which is the most common statistical tool to probe diffusive properties of single-particle trajectories [24]. The TAMSD with the lag time n over a trajectory of

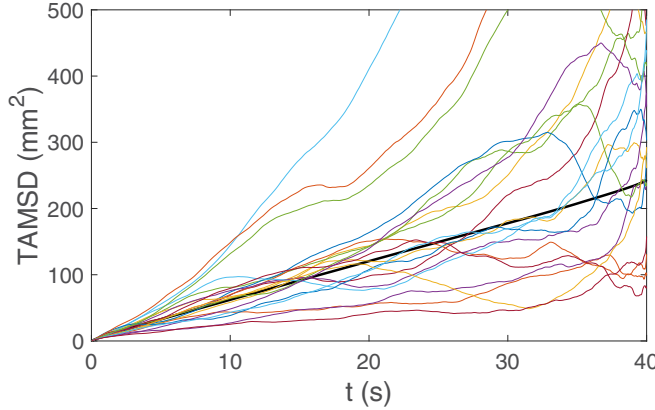


FIG. 7. The time-averaged MSD, $\chi_{n,N}$, as a function of the lag time $t = n\delta$ (with n varying from 1 to 1000), for 20 trajectories of length $N = 1001$ from the sample 1 with the lowest packing fraction. Black thick curve shows the ensemble average of TAMSD over 12 444 trajectories of length $N = 1001$ in this sample. A linear fit of this curve over all lag times n from 1 to 1000 gives the diffusion coefficient of $1.5 \text{ mm}^2/\text{s}$; in turn, its fit over short lag times from 1 to 10 yields $2.3 \text{ mm}^2/\text{s}$.

length N is defined as

$$\chi_{n,N} = \frac{1}{N-n} \sum_{k=1}^{N-n} \|\mathbf{x}_{k+n} - \mathbf{x}_k\|^2. \quad (6)$$

If \mathbf{x}_k are positions of planar Brownian motion with diffusion coefficient D , then the ergodicity of this process implies that

$$\chi_{n,N} \xrightarrow[N \rightarrow \infty]{} 4Dt = 4Dn\delta, \quad (7)$$

whereas the variance of $\chi_{n,N}$ vanishes as $N \rightarrow \infty$ [15,31]. In other words, the TAMSD allows one to estimate the diffusion coefficient D from a *single* random trajectory, and the longer the trajectory, the better the estimation.

For a fixed N , the smallest variance (and thus the best estimation) corresponds to $n = 1$, in which case $\chi_{1,N}$ is the estimator of the variance of increments. This estimator is known to be optimal for the case of Brownian motion; i.e., it is the best possible way to estimate the diffusion coefficient [31–33]. In practice, however, even if the studied particle is supposed to undergo Brownian motion, the acquired trajectory can be altered by various “measurement noises” such as localization error, blur, electronic noise, drift or vibrations of the sample, or postprocessing errors. When some of these noises are anticipated, the estimator can be adapted to provide the (nearly) optimal estimation [18–23,32] (see also Sec. III H). However, the Brownian character of the studied but yet unknown process is not granted and has to be checked from the analysis of the TAMSD. In this situation, the rule of thumb consists in plotting the TAMSD versus the lag time n to first check the linear dependence and then to estimate the diffusion coefficient from the slope of the linear plot. Given the randomness of the TAMSD, this procedure can bring biases and additional statistical errors. Moreover, since fluctuations of the TAMSD grow with n (see [15,31]), the fit is often limited to small n . Figure 7 illustrates large fluctuations of the TAMSD estimator around the ensemble-averaged TAMSD

which exhibits a linear growth with n . As a consequence, an accurate estimation of the diffusion coefficient from a *single* trajectory is only possible over a narrow range of small lag times n . Note that the diffusion coefficient $1.5 \text{ mm}^2/\text{s}$, obtained by fitting the ensemble average (black curve) over all lag times from 1 to 1000, is smaller than that estimated from the standard deviation of one-step increments, $1.8 \text{ mm}^2/\text{s}$ (see Table I). In turn, a linear fit performed over a short window of small lag times from 1 to 10 yields the diffusion coefficient $2.3 \text{ mm}^2/\text{s}$. In Sec. III H, we discuss another estimator of the diffusion coefficient that accounts for localization errors and motion blur.

F. Distribution of TAMSD

One of the significant advantages of single-particle tracking is the possibility to infer information from single events, without ensemble averages. This is particularly important in microbiology because many events in a cell life are triggered by a small number of molecules. Even when many particles are tracked simultaneously, they explore different spatial regions of the cell and experience different interactions with the intracellular environment. If inferred properly, such heterogeneities may bring much more detailed information about the cell than an ensemble average. Performing the estimation for each single trajectory naturally leads to the (empirical) distribution of diffusion coefficients [34–36]. However, it is important to stress that an experimentally obtained distribution includes two sources of randomness: (i) the biological variability and (ii) the intrinsic randomness of the TAMSD estimator obtained from a single finite length trajectory. As a consequence, a proper biological interpretation of such distributions requires disentangling two sources and, ideally, removing the second one. This correction needs the knowledge of the distribution of the TAMSD estimator.

The distribution of TAMSD in the biological context was first studied via numerical simulations by Saxton [37,38]. A more general theoretical analysis of TAMSD for Gaussian processes was later performed in Refs. [31,32,39,40]. We compute the distribution numerically via the inverse Fourier transform of the characteristic function of TAMSD for which the exact matrix formula was provided in Ref. [31]. This computation was shown to be fast and very accurate.

The theoretical distribution of TAMSD for Brownian motion can be compared to the empirical distribution of TAMSD obtained from the trajectories of disks. This comparison allows one to check to which extent the acquired trajectories are close to Brownian motion. Moreover, one can investigate in a well-controlled way how minor deviations from Brownian motion in experimental data can affect this distribution.

Figure 8(a) shows the empirical distribution of TAMSD with the lag time $n = 1$ obtained by splitting each trajectory into fragments of length $N = 100$. This artificial splitting is performed to be closer to the common situation in biological applications, when the acquired trajectories are rather short. Moreover, such splitting significantly improves the statistics of the TAMSD. We compare the probability density functions of TAMSD among 14 samples and with the theoretical curves for Brownian motion. One can see notable deviations from the theoretical distribution, indicating that the acquired

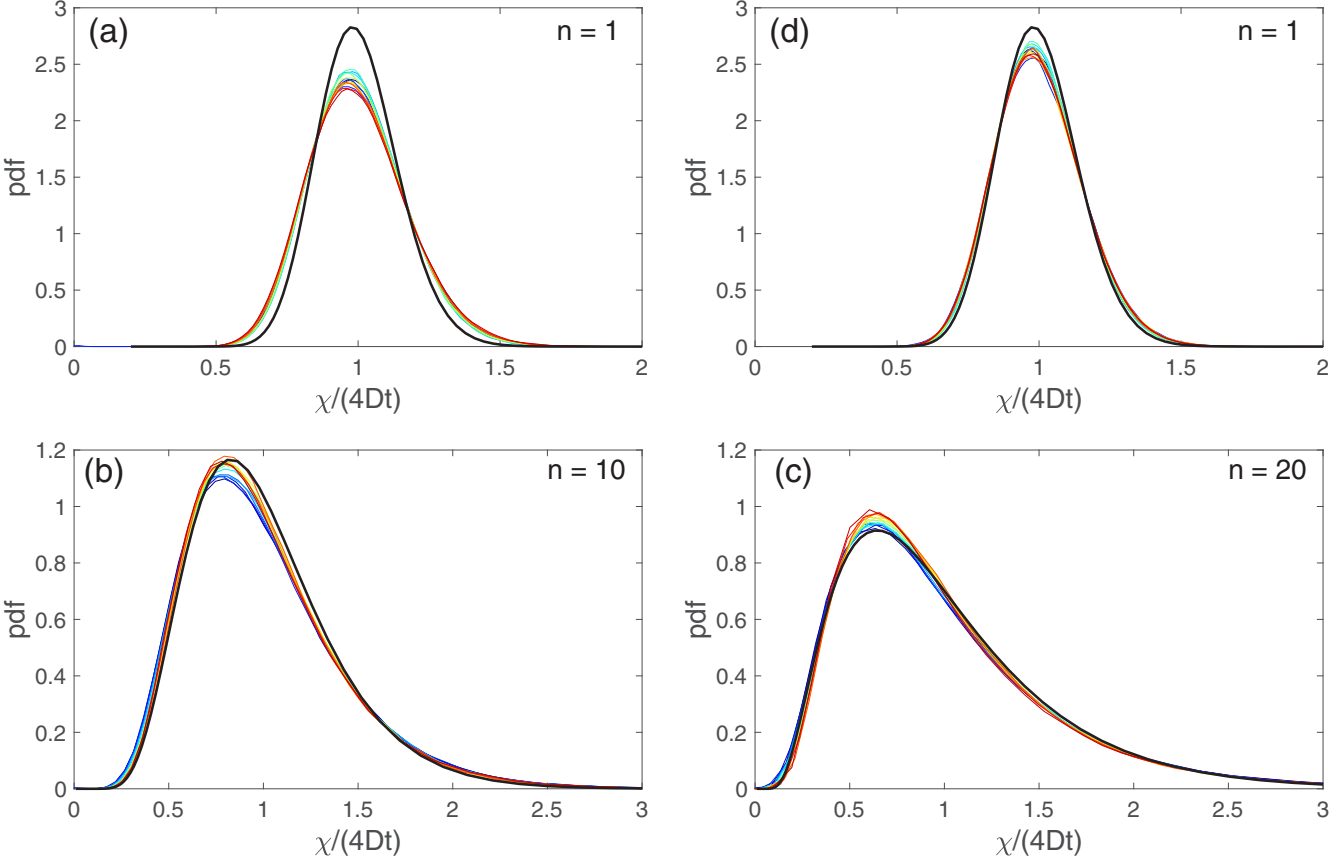


FIG. 8. (a)–(c) Probability density functions of the rescaled TAMSD, $\chi_{n,N}/(4Dt)$, with $N = 100$, $t = n\delta$, and $n = 1$ (a), $n = 10$ (b), and $n = 20$ (c), for 14 samples (thin lines), and the theoretical ones for Brownian motion (thick black line). Color of thin curves changes from dark blue for the lowest packing fraction ϕ to dark red for the highest one. (d) Probability density functions of the rescaled TAMSD with $N = 100$, $t = n\delta$, and $n = 1$, for 14 reshuffled samples.

trajectories are not Brownian, in agreement with the analysis of Sec. III D. The two plausible reasons for the observed deviations are (i) autocorrelations of increments at small lag times (as seen in Fig. 6), and (ii) small deviations from the Gaussian distribution of increments (as seen in Fig. 4). To check for the first reason, we plot in Figs. 8(b) and 8(c) the distributions of the TAMSD with larger lag times $n = 10$ and $n = 20$, at which the VACF was negligible. One gets thus a much better agreement with the theoretical distribution.

In order to check whether the second reason for the deviations (weak non-Gaussianity) is relevant, the increments of all trajectories in each sample were randomly reshuffled to destroy autocorrelations and thus to fully eliminate the first reason for the deviations. New artificial trajectories were constructed from these increments and analyzed. If the original increments were correlated Gaussian variables with the same variance, such a procedure would yield independent identically distributed Gaussian variables so that the resulting trajectories would represent Brownian motion. In this case, a perfect agreement between empirical and theoretical curves would be expected. Figure 8(d) shows empirical and theoretical distributions of TAMSD at the lag time $n = 1$ for reshuffled samples. The agreement is not perfect but is much better than in Fig. 8(a). Small residual deviations can potentially be attributed to weak non-Gaussianity of the distribution of increments.

G. Mean versus the most probable TAMSD

The nonsymmetric shape of the distribution of TAMSD implies that the mean value of the TAMSD is different from its mode, i.e., the most probable value or, equivalently, the position of the maximum of the probability density function (PDF). This difference becomes particularly important for the analysis of single-particle trajectories. When the sample of such individual trajectories is large, the empirical mean of TAMSD estimated from these trajectories is close to the expectation. In turn, when the TAMSD is estimated from a few trajectories (or even from a single trajectory), it is more probable to observe a random realization near the maximum of the PDF. This issue, which was not relevant for symmetric distribution (e.g., a Gaussian distribution), may become an important bias in the analysis of TAMSD.

As discussed in Ref. [31], the distribution of TAMSD for Brownian motion is wider and more skewed for larger n/N . Moreover, the difference between the mean and the mode also grows with n/N . As suggested in [31], the distribution of TAMSD for Brownian motion and some other centered Gaussian processes (like fractional Brownian motion) can be accurately approximated by a generalized gamma distribution, which has a simple explicit PDF,

$$p(z) = \frac{z^{\nu-1} \exp(-a/z - z/b)}{2(ab)^{\nu/2} K_\nu(2\sqrt{ab})} \quad (z > 0), \quad (8)$$

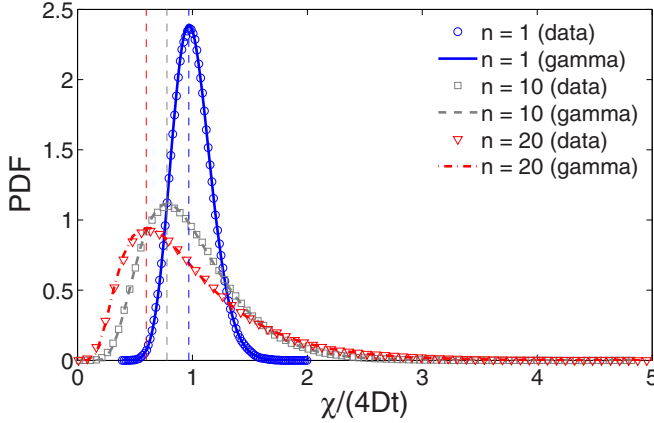


FIG. 9. Probability density functions of the rescaled TAMSD, $\chi_{n,N}/(4Dt)$, for the sample with the lowest packing fraction, with $N = 100$, $t = n\delta$, and $n = 1$ (blue circles), $n = 10$ (gray squares), and $n = 20$ (red triangles). Lines show the generalized gamma distribution $p(z)$ from Eq. (8) whose parameters were obtained from the first three moments (see the text): $a = 3.27$, $b = 0.03$, $v = 28.13$ ($n = 1$), $a = 1.94$, $b = 0.27$, $v = 1.34$ ($n = 10$), and $a = 1.03$, $b = 0.58$, $v = 0.31$ ($n = 20$). The modes of these distributions are shown by vertical dashed lines: 0.97 ($n = 1$), 0.78 ($n = 10$), and 0.60 ($n = 20$), whereas the mean is fixed to be 1 by rescaling.

with three parameters: $a \geq 0$, $b > 0$, and $v \in \mathbb{R}$ [here $K_v(z)$ is the modified Bessel function of the second kind]. The moments of this distribution can be expressed as

$$\langle [\chi_{n,N}]^k \rangle = (ab)^{k/2} \frac{K_{v+k}(2\sqrt{a/b})}{K_v(2\sqrt{a/b})} \quad (k = 1, 2, 3, \dots), \quad (9)$$

whereas the mode is

$$\chi_{n,N}^{\text{mode}} = \frac{\sqrt{(1-v)^2 b^2 + 4ab} - (1-v)b}{2}. \quad (10)$$

For a given empirical distribution of TAMSD, the first three moments, evaluated directly from the data, can be used to calculate the parameters a , b , and v by solving numerically the system of three equations in Eqs. (9) for $k = 1, 2, 3$. In other words, one does not need to fit the empirical distribution in order to get this approximation.

Figure 9 shows the PDF of the TAMSD for the trajectories with the lowest packing fraction, with the sample length $N = 100$ and three lag times, $n = 1$, $n = 10$, and $n = 20$ (shown by symbols). From these empirical data, we evaluated the first three moments and calculated the parameters a , b , and v of the generalized gamma distribution (shown by lines). The excellent agreement validates the use of this theoretical approximation for experimental trajectories. In contrast to Sec. III F, in which we used the exact distribution of TAMSD for Brownian motion, this approximation does not rely on a particular assumption on the underlying stochastic process; it is thus a flexible fitting formula that allows one to approximate the distribution of TAMSD for various processes. In practice, the estimation of the first three moments, from which the parameters a , b , and v are deduced, is much more accurate and easier than the construction of the empirical probability density (i.e., the histogram). In other words, even with a moderate amount of measured TAMSD, which is insufficient

for getting the histogram, one can still estimate the parameters a , b , and v and thus approximate the distribution. As a consequence, the use of the generalized gamma distribution would be particularly valuable in biological applications with a limited number of measurements.

H. Accounting for experimental noises

Single-particle tracking experimental data are unavoidably affected by various measurement noises. The two most common ones are the static localization noise (uncertainty in the detected position of a tracer) and the blurring of the position due to random motion of the tracer between two snapshots. Their effect on the estimated parameters of Brownian motion has been thoroughly investigated [18–21]. In particular, the increment autocorrelation function of one-dimensional Brownian motion was shown to be [19]

$$\mathbb{E}\{\Delta x_k \Delta x_{k+n}\} = \begin{cases} 2D\delta + 2(\sigma_e^2 - 2DR\delta) & (n = 0), \\ -(\sigma_e^2 - 2DR\delta) & (n = 1), \\ 0 & (n > 1), \end{cases} \quad (11)$$

where σ_e^2 is the variance of the localization error (noise) and R is the motion blur coefficient which is determined by the state of the camera shutter during a time lapse δ and can vary between 0 and 1/4. When the camera shutter is kept open for the full duration of the time lapse (as in our experiment), one has $R = 1/6$. When the measurement noises can be neglected (i.e., $\sigma_e = 0$ and $R = 0$), then the diffusion coefficient D can conventionally be estimated from the time average of squared one-step displacements as $\hat{D}_0 = \overline{(\Delta x_k)^2}/(2\delta)$, and this estimation is known to be statistically optimal. In turn, when the measurement noises are comparable to $(\Delta x_k)^2$, the conventional variance estimator may be strongly biased by these noises. Vestergaard *et al.* proposed simple estimators for both the diffusion coefficient D and the noise variance σ_e^2 [21]. Replacing ensemble averages in Eq. (11) by time averages and solving the system of two linear equations yield the estimators

$$\hat{D} = \frac{\overline{(\Delta x_k)^2}}{2\delta} + \frac{\overline{\Delta x_k \Delta x_{k+1}}}{\delta}, \quad (12a)$$

$$\hat{\sigma}_e^2 = R \overline{(\Delta x_k)^2} + (2R - 1) \overline{\Delta x_k \Delta x_{k+1}}, \quad (12b)$$

which were shown to correct for both localization error and blurring and to be optimal for Brownian motion.

We applied the estimator (12a) to the one-step increments of each trajectory of vibrated disks. The empirical mean and standard deviation of such estimated diffusion coefficients are summarized in the last column of Table I. The comparison to the basic estimator \hat{D}_0 shown in the fourth column of the table shows a significant impact of the measurement imperfections on the estimation of the diffusion coefficient. This is not surprising as the estimated resolution on the position of a disk, 0.2 mm (Sec. II), is comparable to the standard deviation of one-step increments, 0.36–0.46 mm (see the third column). The impact of localization error is particularly strong for the increments of a single disk (the first line) and then it is progressively reduced when the packing fraction increases.

This analysis illustrates the importance of accounting for measurement errors. At the same time, we also outline the limitation of such optimal estimators that rely on the strong assumption of the underlying process to be perfect Brownian motion corrupted *only* by localization noise and blurring, whereas other possible imperfections are ignored. For instance, the estimator \hat{D} in Eq. (12a) was deduced from the particular form (11) of the increment autocorrelation function. However, Fig. 6 witnesses that the increments at lag times $n = 2, 3, \dots$ are weakly (anti)correlated. These correlations may also affect the estimation of the diffusion coefficient. As such a process is not, strictly speaking, Brownian motion, one needs first to select an adequate model of the underlying stochastic process and then to develop appropriate statistical tools for calibrating its parameters. An alternative approach consists in using the TAMSD at larger lag times [24,25,32,40]. While this estimation may be suboptimal and has its own limitations (see Sec. III E and Fig. 7), it does not involve specific assumptions on the nature of noises and on the origins of the short-time correlations. In fact, this estimation employs the very basic principle: while local short-time noises provide a constant contribution, the term with the diffusion coefficient increases with the lag time and thus becomes more and more dominant.

IV. CONCLUSION

We proposed a macroscopic realization of planar Brownian motion by vertically vibrated disks. We performed a systematic statistical analysis of many random trajectories of individual disks. The distribution of one-step increments was shown to be close to Gaussian. Small deviations at large increments were shown to increase with the disk packing fraction and thus attributed to interdisk collisions. The velocity autocorrelation function was positive at the lag time $n = 1$ and took negative values at $n > 1$ that rapidly vanish with n . We also analyzed the behavior of the time-averaged mean-squared displacement as a function of the lag time, and its fluctuations from one trajectory to another. We compared the empirical and theoretical distributions of TAMSD and revealed the sensitivity of this distribution at small lag times to eventual autocorrelations and weak non-Gaussianity. We also verified that the empirical distribution can be accurately approximated by the generalized gamma distribution. Finally, we discussed distinctions between the mean TAMSD and the mode of its distribution, and the impact of measurement errors on the estimation of diffusion coefficients. These well-controlled experimental data can serve for validating statistical tools developed for the analysis of single-particle trajectories in microbiology.

ACKNOWLEDGMENTS

D.G. acknowledges the support under Grant No. ANR-13-JSV5-0006-01 of the French National Research Agency.

APPENDIX A: SELECTION BIAS

In this appendix, we investigate the selection bias effect. In order to remove the effect of boundaries of the vibrated plate onto the motion of disk, we have recorded the motion of disks inside the circular ROI of diameter $50d$ in the center of the

vibrated plate. Any trajectory was stopped at the moment of its exit from the ROI, while the disk that reenters the ROI was considered as a new one. This procedure does not yet affect the statistics of motion but only the lengths of trajectories. The selection bias is induced by removing trajectories that are shorter than 1000 points. In fact, if a trajectory was started near the border of the ROI and did not cross this border, its increments are more likely directed towards the center of the ROI. By removing the trajectories that left the ROI (whose increments are more likely directed outwards the ROI), one creates a bias, which can effectively be understood as a small attractive potential toward the center of the ROI.

First, we estimate the fraction of trajectories that were actually removed. If a trajectory is started at radial distance r from the center of the ROI of radius $L = 25d$, it is removed if it exits the ROI at some random time τ which is below $T_{\min} = 1000\delta = 40$ s. In other words, the probability of removing the trajectory is actually the probability that the first exit time τ is below t . For Brownian motion with diffusivity D , the cumulative distribution of the first exit times is well known [41],

$$\mathbb{P}_r\{\tau \leq t\} = 1 - 2 \sum_{k=1}^{\infty} \frac{J_0(\alpha_k r/L)}{\alpha_k J_1(\alpha_k)} \exp(-\alpha_k^2 D t / L^2), \quad (\text{A1})$$

where α_k are the zeros of the Bessel function $J_0(z)$ of the first kind. As we analyze all the disks inside the ROI, the starting point r is uniformly distributed in the ROI. Averaging the above expression over the starting point, we get the probability of removing the trajectory

$$P(t) = \frac{2}{L^2} \int_0^L dr r \mathbb{P}_r\{\tau \leq t\} = 1 - 4 \sum_{k=1}^{\infty} \frac{e^{-\alpha_k^2 D t / L^2}}{\alpha_k^2}. \quad (\text{A2})$$

Setting $D = 2 \text{ mm}^2/\text{s}$ and $L = 25d = 100 \text{ mm}$, one gets $P(T_{\min}) \simeq 0.19$; i.e., 19% of trajectories are affected by this removal procedure.

A priori, such a significant fraction of removed trajectories might lead to the selection bias. However, this is not the case for the distribution of increments. In fact, each trajectory contributes to this distribution a number of increments which is proportional to its length, i.e., $\min\{\tau, T_{\max}\}$, where $T_{\max} = 15\,000$ is the maximal length of the trajectory. As a consequence, the relative number of affected increments can be estimated as

$$\xi = \frac{\int_0^{T_{\min}} dt' t' \rho(t')}{\int_0^{T_{\max}} dt' t' \rho(t') + T_{\max}[1 - P(T_{\max})]}. \quad (\text{A3})$$

The numerator represents the mean number of affected increments (as we remove trajectories that are shorter than T_{\min}), while the denominator is proportional to the mean number of all increments, i.e., $\mathbb{E}\{\min\{\tau, T_{\max}\}\}$, which is expressed in terms of the probability density function $\rho(t) = dP(t)/dt$ of the first passage times to the border of the ROI. Integrating by parts, one gets

$$\begin{aligned} \xi &= \frac{T_{\min} P(T_{\min}) - \int_0^{T_{\min}} dt' P(t')}{T_{\max} - \int_0^{T_{\max}} dt' P(t')} \\ &= \frac{1 - 32 \sum_k \alpha_k^{-2} \left(\frac{DT_{\min}}{L^2} + \alpha_k^{-2} \right) e^{-\alpha_k^2 DT_{\min} / L^2}}{1 - 32 \sum_k \alpha_k^{-4} e^{-\alpha_k^2 DT_{\max} / L^2}}. \end{aligned} \quad (\text{A4})$$

For the considered parameters, we obtain thus $\xi \simeq 0.008$; i.e., the relative fraction of affected increments that may lead to the selection bias is negligible.

Similarly, one can estimate the probability of keeping the trajectory that entered the ROI. In this case, the starting point r is close to the border of the ROI. Setting $r = L - \sigma = 99.6$ mm (with $\sigma = 0.4$ mm) in Eq. (A1), one gets the probability of keeping such a trajectory to be 0.02. In other words, almost all disks that enter the ROI from outside would cross the border again after a number of steps that does not exceed T_{\min} , and all these trajectories are thus removed. We conclude that the selection bias for such trajectories can be neglected.

In order to verify the negligible effect of the selection bias from the trajectories leaving the ROI, we generate a thousand random trajectories of Brownian motion with $D = 2 \text{ mm}^2/\text{s}$ and $\delta = 0.04 \text{ s}$ and apply the same selection procedure as for experimental trajectories. From the ensemble of selected trajectories, we get the empirical distribution of increments which is indistinguishable from the Gaussian one (not shown).

APPENDIX B: ANALYSIS OF SINGLE-DISK TRAJECTORIES

In order to reveal the role of interdisk collisions as compared to intrinsic jumps of disks, we also performed several experiments with a single disk on the vibrated plate. In these measurements, the statistics of trajectories is dramatically reduced, whereas an experimental realization of such a Brownian motion turned out to be even more challenging than with multiple disks because interdisk collisions helped to average out eventual minor imperfections of the experimental setup. In this Appendix, we focus on the distribution of increments estimated from 6 individual trajectories of 18 000 steps each. As for the case with multiple disks, we exclude from the analysis the parts of the trajectory that are beyond the ROI. However, here, we keep even short parts of the trajectory inside the ROI (i.e., we do not apply the former condition on the trajectory length).

Figure 10(a) shows the empirical distribution of rescaled one-step increments. As all increments in this distribution come from the same single trajectory, rescaling by the standard deviation does not affect the statistics and is done only for convenience. First, one can notice that the empirical distributions for six realizations of a single-disk trajectory collapse onto each other, indicating high reproducibility of measurements. As in Fig. 4, the empirical distributions are close to a Gaussian one, except for deviations at large increments. We can therefore conclude that these deviations are related to the intrinsic motion of disks induced by the vibrated plate.

Zooming the region of small increments [see the inset of Fig. 10(a)], one can also notice minor deviations at small increments that were not present in Fig. 4. The observed higher magnitude of the maximum of the distribution can be related to a small number of jumps between two successive acquisitions. In fact, during the lapse time δ , the disk receives 4 kicks from the vibrated plate and thus performs only 4 jumps. If the distribution of each jump is not Gaussian, then the sum of such four random variables is not necessarily Gaussian as the number of variables in the sum is not large enough for the central limit theorem to be applicable.

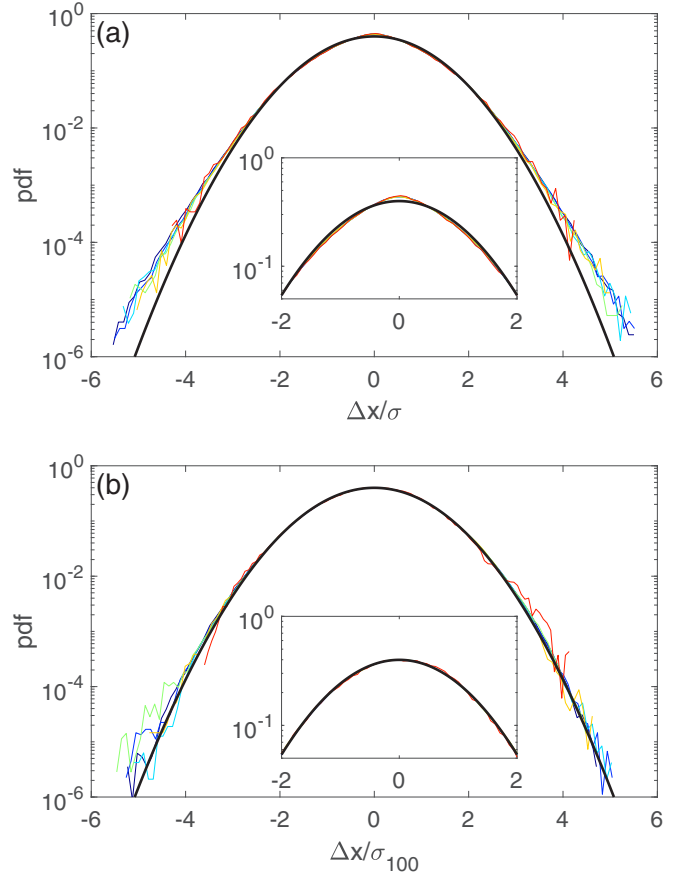


FIG. 10. (a) Empirical distributions of rescaled one-step increments for 6 realizations of a single-disk trajectory. Thick black curve shows the standard Gaussian density $e^{-x^2/2}/\sqrt{2\pi}$. (b) Empirical distributions of rescaled one-hundred-step increments for 6 realizations. Insets show zoomed regions of small increments.

To illustrate this point, one can model the one-step increment along the X coordinate as

$$\Delta x = \sum_{j=1}^J \sigma_j \cos \theta_j, \quad (\text{B1})$$

where J is the number of jumps (in our case, $J = 4$), σ_j are jump lengths, and θ_j are uniformly distributed jump directions. If jumps are independent, the characteristic function of the one-step increment reads

$$\phi(k) = \mathbb{E}\{e^{ik\Delta x}\} = \prod_{j=1}^J \mathbb{E}\{J_0(k\sigma_j)\}, \quad (\text{B2})$$

where the Bessel function $J_0(z)$ comes from the average over uniform jump directions, while the expectation in the last product is taken over σ_j . For instance, if σ_j follow an exponential distribution with the rate λ , then $\mathbb{E}\{J_0(k\sigma_j)\} = \lambda/\sqrt{\lambda^2 + k^2}$, and the probability density of the one-step increment is deduced via the inverse Fourier transform of the characteristic function:

$$P_J(x) = \int_0^\infty \frac{dk}{\pi} \frac{\cos(kx)}{[1 + (k/\lambda)^2]^{J/2}}. \quad (\text{B3})$$

In particular, $P_4(x) = \lambda(1 + \lambda x)e^{-\lambda x}/2$, which is far from Gaussian. While deviations from the Gaussian distributions shown in Fig. 10(a) are much weaker, this toy example illustrates how significant can be lack of multiple jumps between

acquisition times. In turn, these deviations are fully eliminated for the lag time 100, during which the disk receives 400 kicks and the central limit theorem ensures the Gaussian distribution [Fig. 10(b)].

-
- [1] R. Brown, A brief account of microscopic observations made in the months of June, July and August, 1827, on the particles contained in the pollen of plants; and on the general existence of active molecules in organic and inorganic bodies, *Edinburgh New Philos. J.* **5**, 358 (1828).
- [2] J. Perrin, L'agitation moléculaire et le mouvement brownien, *C. R. Hebd. Séances Acad. Sci.* **146**, 967 (1908).
- [3] J. Perrin, Mouvement brownien et réalité moléculaire, *Ann. Chim. Phys.* **18**, 1 (1909).
- [4] E. Frey and K. Kroy, Brownian motion: A paradigm of soft matter and biological physics, *Ann. Phys. (Leipzig)* **14**, 20 (2005).
- [5] D. S. Grebenkov, NMR survey of reflected Brownian motion, *Rev. Mod. Phys.* **79**, 1077 (2007).
- [6] E. Sackmann, F. Keber, and D. Heinrich, Physics of cellular movements, *Annu. Rev. Condens. Matter Phys.* **1**, 257 (2010).
- [7] C. Bräuchle, D. C. Lamb, and J. Michaelis, editors, *Single Particle Tracking and Single Molecule Energy Transfer* (Wiley-VCH, Weinheim, 2010).
- [8] H. M. Jaeger, S. R. Nagel, and R. P. Behringer, Granular solids, liquids, and gases, *Rev. Mod. Phys.* **68**, 1259 (1996).
- [9] J. Choi, A. Kudrolli, R. R. Rosales, and M. Z. Bazant, Diffusion and Mixing in Gravity-Driven Dense Granular Flows, *Phys. Rev. Lett.* **92**, 174301 (2004).
- [10] D. S. Grebenkov, M. P. Ciamarra, M. Nicodemi, and A. Coniglio, Flow, Ordering, and Jamming of Sheared Granular Suspensions, *Phys. Rev. Lett.* **100**, 078001 (2008).
- [11] W. Chen and K. To, Unusual diffusion in a quasi-two-dimensional granular gas, *Phys. Rev. E* **80**, 061305 (2009).
- [12] A. Sarracino, D. Villamaina, G. Gradenigo, and A. Puglisi, Irreversible dynamics of a massive intruder in dense granular fluids, *Europhys. Lett.* **92**, 34001 (2010).
- [13] C. Scalliet, A. Gnoli, A. Puglisi, and A. Vulpiani, Cages and Anomalous Diffusion in Vibrated Dense Granular Media, *Phys. Rev. Lett.* **114**, 198001 (2015).
- [14] L. Walsh, C. G. Wagner, S. Schlossberg, C. Olson, A. Baskaran, and N. Menon, Noise and diffusion of a vibrated self-propelled granular particle, *Soft Matter* **13**, 8964 (2017).
- [15] H. Qian, M. P. Sheetz, and E. L. Elson, Single particle tracking: Analysis of diffusion and flow in two-dimensional systems, *Biophys. J.* **60**, 910 (1991).
- [16] D. Arcizet, B. Meier, E. Sackmann, J. O. Rädler, and D. Heinrich, Temporal Analysis of Active and Passive Transport in Living Cells, *Phys. Rev. Lett.* **101**, 248103 (2008).
- [17] R. Metzler, V. Tejedor, J.-H. Jeon, Y. He, W. H. Deng, S. Burov, and E. Barkai, Analysis of single particle trajectories: From normal to anomalous diffusion, *Acta Phys. Pol. B* **40**, 1315 (2009).
- [18] X. Michalet, Mean square displacement analysis of single-particle trajectories with localization error: Brownian motion in an isotropic medium, *Phys. Rev. E* **82**, 041914 (2010).
- [19] A. J. Berglund, Statistics of camera-based single-particle tracking, *Phys. Rev. E* **82**, 011917 (2010).
- [20] X. Michalet and A. J. Berglund, Optimal diffusion coefficient estimation in single-particle tracking, *Phys. Rev. E* **85**, 061916 (2012).
- [21] C. L. Vestergaard, P. C. Blainey, and H. Flyvbjerg, Optimal estimation of diffusion coefficients from single-particle trajectories, *Phys. Rev. E* **89**, 022726 (2014).
- [22] P. K. Relich, M. J. Olah, P. J. Cutler, and K. A. Lidke, Estimation of the diffusion constant from intermittent trajectories with variable position uncertainties, *Phys. Rev. E* **93**, 042401 (2016).
- [23] M. Lindén, V. Ćurić, E. Amselem, and J. Elf, Pointwise error estimates in localization microscopy, *Nat. Commun.* **8**, 15115 (2017).
- [24] N. Gal, D. Lechtman-Goldstein, and D. Weihns, Particle tracking in living cells: A review of the mean square displacement method and beyond, *Rheol. Acta* **52**, 425 (2013).
- [25] E. Kepten, A. Weron, G. Sikora, K. Burnecki, and Y. Garini, Guidelines for the fitting of anomalous diffusion mean square displacement graphs from single particle tracking experiments, *PLoS ONE* **10**, e0117722 (2015).
- [26] M. Magdziarz and A. Weron, Anomalous diffusion: Testing ergodicity breaking in experimental data, *Phys. Rev. E* **84**, 051138 (2011).
- [27] Y. Lanoiselée and D. S. Grebenkov, Revealing nonergodic dynamics in living cells from a single particle trajectory, *Phys. Rev. E* **93**, 052146 (2016).
- [28] Y. Lanoiselée and D. S. Grebenkov, Unraveling intermittent features in single particle trajectories by a local convex hull method, *Phys. Rev. E* **96**, 022144 (2017).
- [29] J. Deseigne, S. Léonard, O. Dauchot, and H. Chaté, Vibrated polar disks: Spontaneous motion, binary collisions, and collective dynamics, *Soft Matter* **8**, 5629 (2012).
- [30] See Supplemental Material at <http://link.aps.org/supplemental/10.1103/PhysRevE.98.062112> for three video files showing the experiment with a single disk (video-phi0.avi) and two experiments at packing fractions 0.40 (video-phi040.avi) and 0.637 (video-phi0637.avi).
- [31] D. S. Grebenkov, Probability distribution of the time-averaged mean-square displacement of a Gaussian process, *Phys. Rev. E* **84**, 031124 (2011).
- [32] D. S. Grebenkov, Optimal and suboptimal quadratic forms for noncentered Gaussian processes, *Phys. Rev. E* **88**, 032140 (2013).
- [33] H. Cramér, *Mathematical Methods of Statistics* (Princeton University Press, Princeton, 1946).
- [34] M. H. G. Duits, Y. Li, S. A. Vanapalli, and F. Mugele, Mapping of spatiotemporal heterogeneous particle dynamics in living cells, *Phys. Rev. E* **79**, 051910 (2009).
- [35] M. Otten, A. Nandi, D. Arcizet, M. Gorelashvili, B. Lindner, and D. Heinrich, Local motion analysis reveals impact of the

- dynamic cytoskeleton on intracellular subdiffusion, *Biophys. J.* **102**, 758 (2012).
- [36] A. Nandi, D. Heinrich, and B. Lindner, Distributions of diffusion measures from a local mean-square displacement analysis, *Phys. Rev. E* **86**, 021926 (2012).
- [37] M. J. Saxton, Lateral diffusion in an archipelago: Single-particle diffusion, *Biophys. J.* **64**, 1766 (1993).
- [38] M. J. Saxton, Single-particle tracking: The distribution of diffusion coefficients, *Biophys. J.* **72**, 1744 (1997).
- [39] A. Andreanov and D. S. Grebenkov, Time-averaged MSD of Brownian motion, *J. Stat. Mech.* (2012) P07001.
- [40] G. Sikora, M. Teuerle, A. Wyłomanska, and D. S. Grebenkov, Statistical properties of the anomalous scaling exponent estimator based on time-averaged mean-square displacement, *Phys. Rev. E* **96**, 022132 (2017).
- [41] S. Redner, *A Guide to First Passage Processes* (Cambridge University Press, Cambridge, England, 2001).